Engineering 43 (2024) 72–80

Contents lists available at ScienceDirect

Engineering

journal homepage: www.elsevier.com/locate/eng

Research
Advanced Antennas for Wireless Connectivity—Article

The Low-Attenuation Endfire Leaky-Wave State on an Optically Transparent Lossy Film

Ziheng Zhou [a,b], Yongjian Zhang [b], Yilin Zheng [c], Ke Chen [d], Yueming Gao [a], Yuehe Ge [a], Yue Li [b,*], Yijun Feng [d,*], Zhizhang (David) Chen [a,e,*]

[a] College of Physics and Information Engineering, Fuzhou University, Fuzhou 350108, China
[b] Department of Electronic Engineering, Tsinghua University, Beijing 100084, China
[c] School of Electronic and Information Engineering, Soochow University, Soochow 215006, China
[d] School of Electronic Science and Engineering, Nanjing University, Nanjing 210023, China
[e] Department of Electrical and Computer Engineering, Dalhousie University, Halifax, NS B3H 4R2, Canada

ARTICLE INFO

Article history:
Received 22 December 2023
Revised 11 August 2024
Accepted 2 September 2024
Available online 28 September 2024

Keywords:
Antennas
Endfire radiation
Low attenuation
Material losses
Transparent conductive films

ABSTRACT

The development of high-performance optically transparent radio frequency (RF) radiators is limited by the intrinsic loss issue of transparent conductive films (TCFs). Instead of pursuing expensive endeavors to improve the TCFs' electrical properties, this study introduces an innovative approach that leverages leaky-wave mode manipulation to mitigate the TCFs' attenuating effect and maximize the RF radiation. Our finding reveals that the precise control of the mode confinement on glass-coated TCFs can create a low-attenuation window for leaky-wave propagation, where the total attenuation caused by TCF dissipation and wave leakage is effectively reduced. The observed low-attenuation leaky-wave state on lossy TCFs originates from the delicate balance between wave leakage and TCF dissipation, attained at a particular glass cladding thickness. By leveraging the substantially extended radiation aperture achieved under suppressed wave attenuation, this study develops an optically transparent antenna with an enhanced endfire realized gain exceeding 15 dBi and a radiation efficiency of 66%, which is validated to offer competitive transmission performance for advancing ubiquitous wireless communication and sensing applications.

1. Introduction

Converting radio frequency (RF) power from a source or guided-wave structure into free-space radiation [1,2] is a fundamental topic in physics and engineering. This process plays a pivotal role in a broad spectrum of applications such as wireless communication [2,3], wireless power transfer [2,4], remote sensing [5], and biomedical imaging [6,7]. Intensive research has been dedicated to the generation and regulation of RF radiation via radiators (i.e., antennas) constructed with opaque metallic layers or patterns [2], leading to the emergence of radiator designs based on leaky-wave structures [8–16], open resonators [17–21], and artificially engineered materials [22–24]. In recent years, the concept of optically transparent antennas (OTAs) [25–30] has garnered significant interest from both academia and industry. OTAs are expected to fulfill the same fundamental functions as their traditional, opaque counterparts in transmitting (Tx) and receiving (Rx) radio waves without affecting the utilization of visible light resources [25–28]. Specifically, they can be invisibly integrated into various transparent platforms, such as windows [31,32], solar panel shields [33–35], and display screens [36–39], offering promising opportunities for ubiquitous wireless communication and sensing applications.

To implement the concept of OTAs, transparent conductors—which are commonly in the form of transparent conductive films (TCFs)—are of vital importance. Two major categories of TCFs have been developed, which are transparent-conductive-oxide films [25,40–42] and meshed metal films [25,43–48]. The transparent-conductive-oxide films, such as indium-tin-oxide (ITO) film [38–40], take advantage of decent optical transmittance and can be easily mass-produced via deposition technologies [25,40,41]. Nevertheless, the high sheet resistance of transparent-conductive-oxide

* Corresponding authors.
E-mail addresses: lyee@tsinghua.edu.cn (Y. Li), yjfeng@nju.edu.cn (Y. Feng), z.chen@dal.ca (Z. (David) Chen).

https://doi.org/10.1016/j.eng.2024.09.014

films, typically a few ohms per square ($\Omega{\cdot}sq^{-1}$) in the RF region [25,40–42], poses a significant challenge for realizing high radiation performance. The meshed metal films, on the other hand, can offer a lower sheet resistance in an order of 0.5 $\Omega{\cdot}sq^{-1}$ [25,43–48]. However, the diffraction of light caused by the micro-sized metal grids would have detrimental effects on optical imaging and display [38].

The difficulty for a thin conductive film to achieve both high optical invisibility and low sheet resistance originates from the mutual constraint between the optical transmittance and carrier density [28,39–41]. To enhance the optical transmittance of a homogeneous TCF, it is a feasible approach to lower its plasma frequency (i.e., the threshold frequency allowing the passage of light) below the visible-light range. This however requires smaller carrier density and hence leads to reduced electrical conductivity [39–41]. For this reason, TCFs are also known as optically transparent lossy films [25,40]. The intrinsic loss issue of TCFs has been shown to severely constraint the performance of optically transparent radiators [25–27,31,32,37–39,46,49–55]. First, the significant ohmic dissipation in TCFs can reduce the radiation efficiency, which is defined by the ratio of radiated power to the power accepted by the radiator. Additionally, the rapid decay of electromagnetic waves in lossy TCF structures hinders the creation of an electrically large aperture for generating directive radiation. As a key metric, the gain of a radio-wave radiator qualifies its ability to concentrate radiation power in a specific direction [2]. Due to the limited radiation efficiency and directivity caused by TCF losses, most existing designs of OTAs [25–27,31,32,37–39,46,49–55] exhibit significantly lower gains than their opaque metal-based counterparts. To improve the OTA's radiation performance, Song et al. [56] proposed to selectively metalize the structure edges with high current density, which increased the antenna's gain from −5 to 0 dBi and efficiency from 38% to 68%. Moreover, the gold nanolayer deposition [57] was introduced to improve the OTA's efficiency, but this degraded the OTA's optical transparency inevitably.

The inherent contradiction between the high optical transmittance and low sheet resistance of TCFs [39,40,58] renders it challenging to improve OTAs' radiation performance solely through the effort of material science. In this study, we present a new approach that manipulates electromagnetic leaky-wave mode for suppressing the attenuation effect of TCFs. Our finding shows that for a thin TCF-grounded glass slab waveguide (GSW), the radio-wave power carried by its fundamental transverse-magnetic (TM) propagation mode is predominantly distributed in the air region rather than being confined near the TCF, which effectively suppresses the ohmic loss on the TCF. Nontrivially, we uncover that the total attenuations due to TCF loss and wave leakage can be substantially minimized at a unique glass-slab thickness, which ratifies the existence of a low-attenuation mode and provides a unique condition for high-gain endfire radiation. The prototyped transparent leaky-wave antenna features an extended aperture size of $7.9\lambda_0 \times 1.9\lambda_0$ (λ_0 is the free-space wavelength at the frequency f_0 = 8.6 GHz) and optical transmittance higher than 80%, and it is verified to deliver an exceptionally high realized gain of 15.2 dBi and a radiation efficiency of 66% at f_0. Furthermore, a wireless image transfer experiment is conducted to validate the excellent transmission performance of the proposed OTA. Owing to the optical transparency and high-gain endfire radiation performance, the proposed antenna can be integrated onto vehicular roof glasses, serving for communicating with the front targets and detecting the obstacles in the way. In essence, this study creates a pathway for realizing OTAs with high gain and improved efficiency, offering promising prospects for widespread applications in wireless communication and sensing.

2. Concept and theory

To start with, we investigate the fundamental characteristics of radio waves propagating in a TCF-grounded GSW, which is an optically transparent leaky-wave structure featuring a simple configuration. This structure consists of a glass slab with a thickness of h and a relative permittivity of ε_r, grounded by a TCF with a sheet resistance of R_s. The TCF-grounded GSW structure features a compact profile only half that of a pure dielectric waveguide. Additionally, the grounding also effectively eliminates RF power leakage beneath the dielectric waveguide, thus avoiding the potential risk of RF field exposure when the OTA is mounted on vehicle glasses. As illustrated in Figs. 1(a)–(c) and theoretically interpreted in what follows, the confinement and attenuation behavior of the wave on the TCF-grounded GSW can be effectively controlled via adjusting the glass-slab thickness h. This adjustment yields an optimal solution for minimizing the total attenuation constant caused by the power leakage and TCF dissipation, essential for extending the leaky-wave radiation aperture and maximizing the realized gain in the GSW's endfire direction (as illustrated in Fig. 1(b)).

As shown in Figs. 1(a)–(c), for a two-dimensional (2D) TCF-grounded GSW extending along the +y axis, electromagnetic fields of its TM modes exhibit cosinusoidal or sinusoidal variation along the transverse direction (+z axis) in the glass slab ($0 < z < h$), while exhibiting an exponentially decaying behavior along the +z axis in the air ($z > h$) [59]. As derived in Appendix A Section S1, the dispersion equation for its phase constant β under TM modes is given by

$$\varepsilon_r\sqrt{\beta^2-k_0^2}=\sqrt{\varepsilon_r k_0^2-\beta^2}\tan\left(\sqrt{\varepsilon_r k_0^2-\beta^2}h\right) \tag{1}$$

where k_0 represents the wave number in free space. For the fundamental TM_1 propagation mode of the TCF-grounded GSW, its phase constant β can be solved from Eq. (1) and asymptotically expressed by

$$\beta\approx k_0\left[1+\frac{1}{2}\left(\frac{\varepsilon_r-1}{\varepsilon_r}\right)^2 k_0^2h^2\right] \tag{2}$$

when h is significantly smaller than the free-space wavelength λ_0. Eq. (2) intuitively indicates that a thicker GSW can lead to an increased phase constant, or equivalently, a reduced phase velocity. Here, we denote the power transmitted in the air and glass slab as P_{air} and P_{slab}, respectively, and the total transmitted power in the TCF-grounded GSW as $P_{total} = P_{air} + P_{slab}$. The explicit expressions for P_{air} and P_{slab} are provided in Section S1. The theoretically calculated power ratios P_{air}/P_{total} and P_{slab}/P_{total} that depend on the normalized glass-slab thickness h/λ_0 are shown in Fig. 1(d). This figure shows that, as glass-slab thickness increases, the transmitted power tends to be confined within the glass slab rather than distributed into the air.

The ability to control the power distribution in the air and glass enables the confinement of waves in TCF-grounded GSWs to be regulated, which further allows the wave attenuation and leakage properties to be fine-tuned. The perturbation method [60] is applied to calculate the attenuation constants α_{TCF} and α_{rad}, which measure power decay due to the TCF loss and power leakage, respectively. As derived in Appendix A Section S2, the explicit expression of the attenuation coefficient α_{TCF} is

$$\alpha_{TCF}=\frac{\omega\varepsilon_0\varepsilon_r^2R_s}{\varepsilon_r\beta h\left[1+\frac{\sin(2Th)}{2Th}\right]+\frac{\beta[\sin(Th)]^2T^2}{\tau^3}} \tag{3}$$

where ε_0 is the permittivity of vacuum, and ω is the angular frequency; T and τ denote the transverse wave numbers in the glass-slab and air regions, respectively. The calculated results of α_{TCF} for the TCF's sheet resistance R_s = 3 $\Omega{\cdot}sq^{-1}$ and different

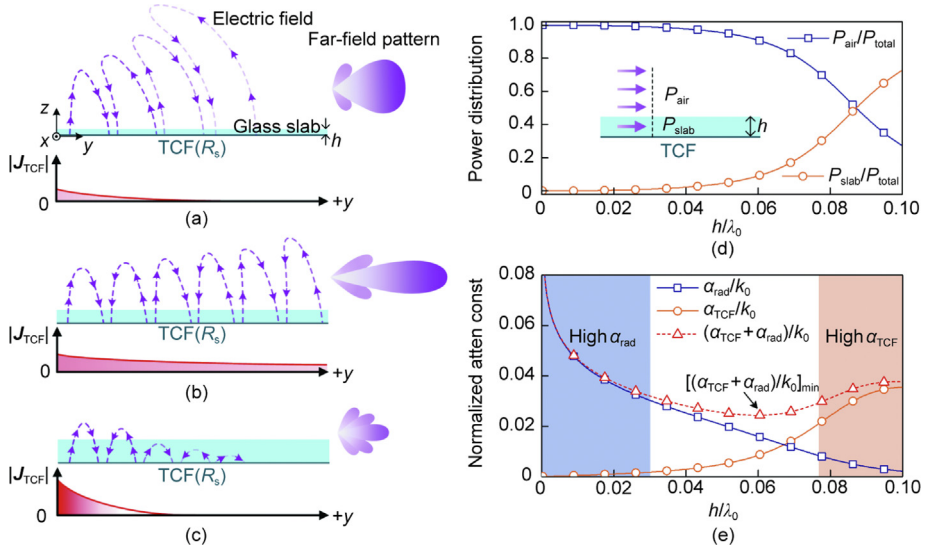

Fig. 1. Demonstration for finding the low-attenuation leaky-wave state on a lossy TCF. (a–c) Schematic plots of electric field and current distributions along with far-field radiation patterns of TCF-grounded GSW with different thicknesses. (d, e) Theoretically calculated (d) proportions of powers distributed in different regions and (e) normalized attenuation constants due to TCF loss and leakage radiation. Results are given under the relative permittivity of the lossless glass slab chosen as ε_r = 7.3, the TCF's sheet resistance R_s = 3 Ω·sq^{-1}, and frequency f_0 = 8.6 GHz. P_{air}: the power transmitted in the air; P_{slab}: the power transmitted in the glass slab; P_{total}: the total transmitted power in the TCF-grounded GSW; k_0: the wave number in free space; $\boldsymbol{J}_{TCF}$: surface current density on TCF; α_{rad}: attenuation constant due to leakage radiation; α_{TCF}: attenuation constant due to TCF loss; atten const: attenuation constant.

normalized glass-slab thicknesses h/λ_0 are represented by the solid line with circle markers shown in Fig. 1(e). The TCF-loss-induced attenuation coefficient increases with the normalized glass-slab thickness h/λ_0 because of enhanced field confinement near the TCF. Because most of the power distributed in the air region is hardly captured by the height-limited Rx port, it would predominantly contribute to the endfire leaky-wave radiation. The attenuation constant describing the leakage radiation is therefore approximately evaluated by $\alpha_{rad} = -[1/(2L)] \times \ln[(P_{total} - P_{air})/P_{total}]$, where an exponential decay of power is assumed and the GSW length L is set as $9.2\lambda_0$. As derived in Section S2, the explicit expression of the attenuation constant α_{rad} is given as

$$\alpha_{rad} = -\frac{1}{2L}\ln\left\{\frac{1+\mathrm{sinc}\ (2Th)}{1+\mathrm{sinc}\ (2Th)+[T^4h/(\varepsilon_r\tau^3)]\mathrm{sinc}^2(Th)}\right\} \quad (4)$$

which is depicted in Fig. 1(e) and indicates that α_{rad} is inversely related to the normalized glass-slab thickness h/λ_0. The total attenuation constant $\alpha_{TCF} + \alpha_{rad}$ is then calculated and represented by the dashed curve shown in Fig. 1(e). Thus, both excessively thin and thick GSW can lead to a relatively high total attenuation, which is attributed to either large radiation-induced attenuation α_{rad} or large TCF-loss-induced attenuation α_{TCF}. The rapidly decaying electric field and current distributions in these two cases are schematically illustrated in Figs. 1(a) and (c), respectively. For a glass slab with a vanishing thickness (shown in Fig. 1(a)), the weak wave confinement of the GSW leads to a rapid escape of power into free space, which manifests as a high leakage-induced attenuation. At the other extreme, for an excessively thick glass slab (shown in Fig. 1(c)), the strong confinement of the wave near the TCF induces an intensified and locally distributed surface current $|\boldsymbol{J}_{TCF}|$, causing high ohmic dissipation. As an exceptional effect observed in Fig. 1(e), a minimized total attenuation constant is attained by tuning the glass-slab thickness close to $0.06\lambda_0$. This special point corresponds to a balanced power leakage and material dissipation achieved at an optimal wave confinement level, which in turn maximizes the wave propagation distance on the TCF.

By leveraging the TCF-grounded GSW designed for suppressing total attenuation of the wave, we propose an approach to generate high-gain radiation on a lossy TCF. To focus the electromagnetic power in a specific direction (i.e., to realize a high gain), both an electrically large aperture and high radiation efficiency are required. A TCF-grounded GSW with an excessively small (or large) thickness as shown in Fig. 1(a) (or Fig. 1(c)) can only offer a very limited aperture size owing to its excessively large power leakage rate (or TCF-induced attenuation). Furthermore, an excessively thick TCF-grounded GSW exhibits low radiation efficiency owing to significant TCF losses. Consequently, the antenna gains in these two cases (shown in Figs. 1(a) and (c)) remain low. Nevertheless, once the GSW structure is designed under the condition in which the total attenuation is suppressed (shown in Fig. 1(b)), a substantially increased aperture size and improved radiation efficiency can be achieved simultaneously, which maximizes the realized gain of RF radiation excited on the TCF.

3. Numerical analysis

To interpret the theory of the low-attenuation leaky-wave mode in a TCF-grounded GSW, this section numerically investigates a three-dimensional (3D) TCF-grounded GSW structure consisting of a lossy glass slab. The full-wave analysis is carried out using the numerical software Ansys HFSS® (ANSYS, USA), and the details of the numerical simulation are reported in Appendix A Section S3. Fig. 2(a) shows the structure of a TCF-grounded GSW with thickness h and connected to two stepped transitions. The glass slab constituting the GSW is characterized by a relative permittivity of 7.3 and a loss tangent (tanδ) of 0.008, and the sheet resistance of the TCF ground is set as 3 Ω·sq^{-1}. The upper two layers of stepped transitions are composed of quartz glass with a relative permittivity of 3.75. Power excitation is applied at the waveguide (WG) port 1 (P_1), and port 2 (P_2) serves to receive the residue power. Fig. 2(b) displays the simulated electric-field intensity distributions on the y–z cut plane at f_0 = 8.6 GHz for the glass-slab thickness values of 0.7 ($0.020\lambda_0$), 2.0 ($0.057\lambda_0$), and 2.6 mm

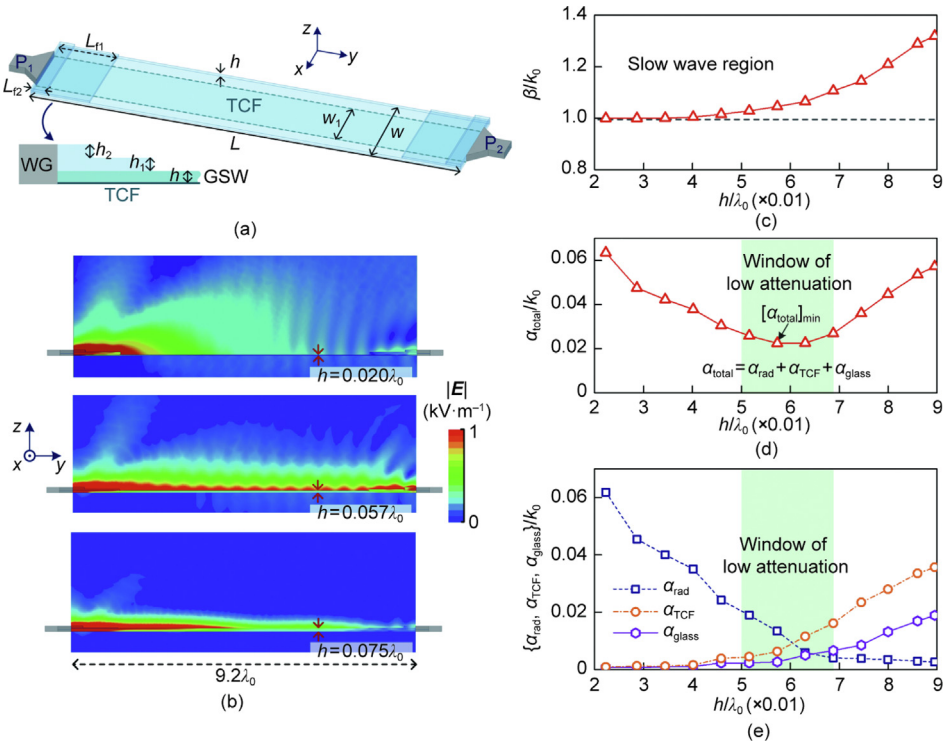

Fig. 2. Numerical analysis of propagation characteristics in a TCF-grounded GSW. (a) 3D TCF-grounded GSW structure. The feeding waveguide (WG) port sizes are 16.0 mm × 5.3 mm. (b) Simulated electric-field magnitude distributions for different glass-slab thicknesses h at f_0 = 8.6 GHz on the y–z cut plane. The power put into the GSW is 1 W and $|\boldsymbol{E}|_{max}$ = 1 kV·m^{-1}. (c, d) Numerically computed (c) phase constant and (d) total attenuation constant at f_0 dependent on glass-slab thicknesses h. (e) Attenuation constants describing leakage radiation, TCF loss, and glass loss. L: GSW length (L = 320 mm); w: width of the glass substrate (w = 66 mm); w_1: width of the TCF (w_1 = 42 mm); h_1 and h_2: heights of the first- and second-layer quartz glasses, being 1.5 and 2.0 mm, respectively; L_{f1} and L_{f2}: lengths of the first- and second-layer quartz glasses, being 44 and 11 mm, respectively; P_1: waveguide port 1; P_2: waveguide port 2; α_{total}: total attenuation constant; α_{glass}: attenuation constant due to the dielectric loss in glass.

(0.075λ_0). As seen, the excessively thin GSW structure with h = 0.020λ_0 causes a rapid leakage of power, which significantly limits the propagation distance of the wave. At the other extreme, an excessively thick glass slab (h = 0.075λ_0) leads to overly strong wave confinement that intensifies the attenuating effect of lossy TCF. As an exceptional case shown in the middle subfigure of Fig. 2(b), by adjusting the GSW's thickness to 0.057λ_0, a low-loss propagation state with a substantially reduced total attenuation constant is achieved, which yields a maximized wave propagation distance.

Fig. 2(c) shows the phase constant of the 3D TCF-grounded GSW extracted from the instantaneous electric field distribution. The results are given at a fixed frequency of 8.6 GHz and for various glass-slab thicknesses h. As shown in Fig. 2(c), the GSW with a thicker glass slab yields a larger phase constant, which agrees with the theoretical result given by Eq. (2). The enhanced slow-wave effect implies that the propagation mode tends to become more confined near TCF as the slab thickness increases. The total attenuation constant α_{total} for the propagation in the TCF-grounded GSW structure is retrieved from the transmission and reflection coefficients, and the result is presented in Fig. 2(d). The total attenuation constant α_{total} can be broken down into components corresponding to leakage radiation, ohmic loss of TCF, and dielectric loss of glass; namely, $\alpha_{total} = \alpha_{rad} + \alpha_{TCF} + \alpha_{glass}$. The procedure to numerically compute attenuation constants α_{rad}, α_{TCF}, and α_{glass} is presented in Appendix A Section S4, and Appendix A Fig. S1 shows attenuation constants of involved cases with different material settings. Fig. 2(e) shows the dependence of extracted α_{rad}, α_{TCF}, and α_{glass} on the glass-slab thickness h at f_0 = 8.6 GHz. As the glass-slab thickness h increases, the radiation-induced attenuation constant α_{rad} decreases because of the enhanced wave confinement. Nevertheless, the enhanced wave confinement in turn causes increased power dissipation in the lossy TCF and glass slab, leading to increases in α_{TCF} and α_{glass}. By carefully selecting the glass slab thickness to attain a balance between radiation-induced and lossy-material-induced attenuations, a "low-attenuation window"—represented by the green shaded region in Fig. 2(e)—can be created, which explains the existence of the minimum-total-attenuation point.

4. Antenna design and measurement

By leveraging the low-attenuation leak-wave state in a transparent TCF-grounded GSW, we propose the design of an optically transparent high-gain leaky-wave antenna, as shown in Fig. 3(a). This antenna structure is based on the TCF-grounded GSW presented in Fig. 2(a), with the excitation structure assigned only at the left end. To maximize the antenna gain, the selection of glass-slab thickness h should consider two factors. First, to achieve a significantly extended radiation aperture, the TCF-grounded GSW should operate near the critical point of minimum total attenuation to enable low-loss leaky-wave propagation. Second, it is necessary to maintain a high radiation efficiency by using an adequate power leakage rate (α_{rad}), which is more easily attainable with a thinner GSW. In our theoretical model for evaluating the antenna's realized gain, the aperture fields are assumed to be uniformly distributed along the x-axis over an effective aperture width of w_{eff}, while propagating along the y-axis with a complex propagation constant of $\beta - j\alpha_{total}$ (where j is the imaginary unit). The schematic illustration of the aperture current distribution is shown in Appendix A Fig. S2, and as derived in Appendix A

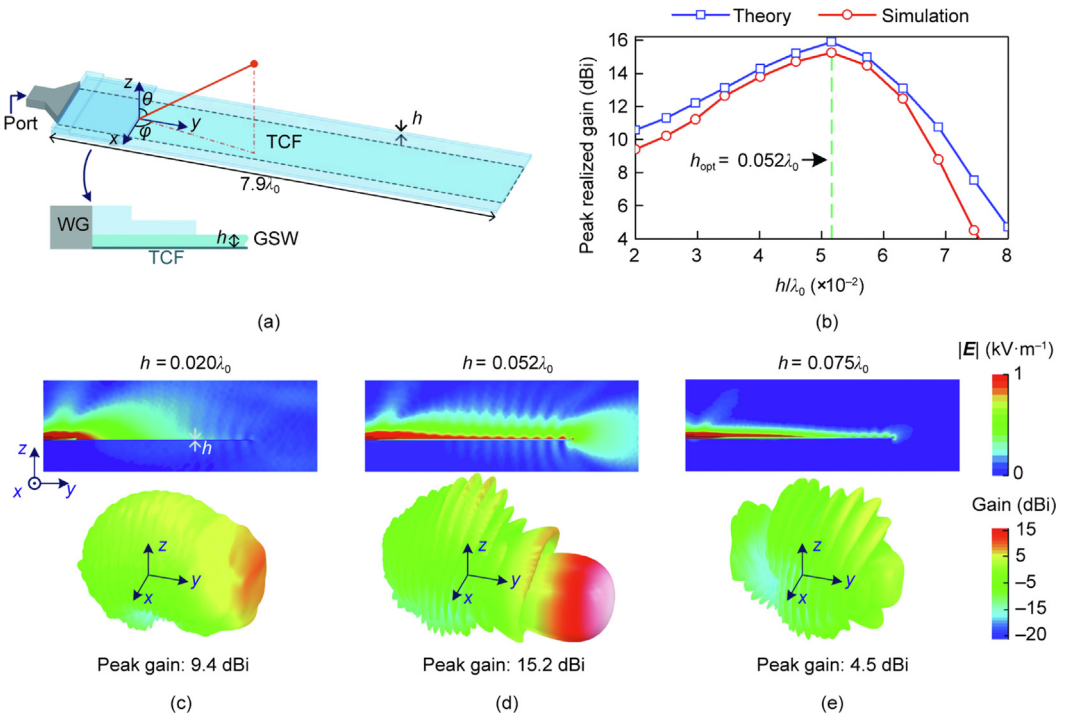

Fig. 3. Demonstration of the optimal-gain design of the optically transparent endfire leaky-wave antenna. (a) Structure of the proposed transparent leaky-wave antenna. (b) Theoretically and numerically calculated peak antenna realized gain in space (at f_0 = 8.6 GHz) dependent on the glass-slab thickness h. (c–e) Numerically simulated electric-field magnitude distributions and 3D realized gain distributions of the optically transparent leaky-wave antennas with $h = 0.020\lambda_0$, $0.052\lambda_0$, and $0.075\lambda_0$. The TCF and glass slab widths follow the setting given in Fig. 2. φ: the azimuth angle; θ: the elevation angle; h_{opt}: the optimal glass-slab thickness.

Section S5, the angular distribution of realized gain G of the antenna for a given glass-slab thickness h is

$$G(\theta,\varphi;h)=\eta\cdot\lim_{|\boldsymbol{r}|\to\infty}\frac{4\pi|\boldsymbol{r}|^2|\boldsymbol{E}(\boldsymbol{r})|^2}{\oint|\boldsymbol{r}|^2|\boldsymbol{E}(\boldsymbol{r})|^2\mathrm{d}\Omega}=\eta\frac{\mathrm{sinc}^2\left[k_0\frac{w_{\mathrm{eff}}}{2}\sin\theta\cos\varphi\right]}{\left[\sin\theta\sin\varphi-\beta/k_0\right]^2+\left(\alpha_{\mathrm{total}}/k_0\right)^2}\times\frac{\sin^2\theta\sin^2\varphi+\cos^2\theta}{C(\beta,\alpha_{\mathrm{total}})}\tag{5}$$

where θ and φ are respectively the elevation and azimuth angles, $\boldsymbol{E}$ is the electric field, $\boldsymbol{r}$ is the position vector of the observation point, η is the antenna's total efficiency, and $C(\beta,\alpha_{\mathrm{total}})$ is the normalized factor. On the slow-wave operating region of the grounded GSW, the antenna's realized gain pattern $G(\theta,\varphi;h)$ in Eq. (5) reaches its peak value in the endfire direction of $\theta = 90°$ and $\varphi = 90°$, and the optimal glass-slab thickness h_{opt} is hence determined via

$$h_{\mathrm{opt}}=\underset{h}{\mathrm{argmax}}\left[\max_{\theta\in[0,\pi],\varphi\in[0,2\pi]}G(\theta,\varphi;h)\right]=\underset{h}{\mathrm{argmax}}\left[G(\theta=90°,\ \varphi=90°;h)\right]\tag{6}$$

Fig. 3(b) shows the theoretically calculated antenna peak realized gain in space along with the numerical simulation results, which are presented as a function of the normalized glass-slab thickness. Both the theoretical and simulation results indicate that the antenna's peak realized gain in space reaches a maximum value surpassing 15 dBi at the optimal thickness $h_{opt} = 0.052\lambda_0$. This optimal solution falls within the low attenuation window (i.e., the shaded region in Fig. 2(d), and approaches the point of minimum total attenuation marked in the figure).

To shed light on the formation of the optimal-gain radiation, Figs. 3(c)–(e) show simulated electric-field distributions and 3D realized gain distributions for the glass-slab thicknesses of 0.7 ($0.020\lambda_0$), 1.8 ($0.052\lambda_0$), and 2.6 mm ($0.075\lambda_0$), respectively. As shown in Fig. 3(c), for the excessively thin ($h = 0.020\lambda_0$) GSW with a large power leakage rate α_{rad}, the rapid decay of leaky wave power over a short distance contributes to a broad radiation beam with a low peak realized gain. At the other extreme, for an excessively thick GSW ($h = 0.075\lambda_0$), as shown in Fig. 3(e), the enhanced wave confinement near the lossy TCF significantly increases the TCF attenuation, which in turn limits the aperture size and radiation efficiency. By tuning the glass-slab thickness to the optimal value of $0.052\lambda_0$, obtain a directive radiation pattern with a high realized gain exceeding 15 dBi is obtained, as shown in Fig. 3(d). This significantly enhanced gain is achieved because an appropriate power leakage rate and low material attenuation are attained simultaneously. As shown in Appendix A Fig. S3, for the 8.0–9.0 GHz frequency range, the GSW-loaded antenna exhibits a 9.5 dB realized gain improvement compared to the metallic feeding horn, which also demonstrates the effectiveness of the proposed design. The numerical parametric study results of the proposed antenna with $h = 0.052\lambda_0$ and different widths are shown in Appendix A Fig. S4, which indicates that, given a feeding waveguide width of 16 mm, selecting GSW width parameters of w = 66 mm ($1.89\lambda_0$) and w_1 = 42 mm ($1.20\lambda_0$) ensures the optimal realized gain.

Fig. 4(a) shows the prototype of the optically transparent leaky-wave antenna that was fabricated according to the optimal-gain design. The TCF-grounded GSW is constructed using a 1.8 mm-thick soda-lime glass slab with $\varepsilon_r = 7.3$ and $\tan\delta = 0.008$, which is grounded by an ITO film. The ITO film has a thickness of 400 nm and sheet resistance of 3 $\Omega\cdot\mathrm{sq}^{-1}$, which is deposited by using the magnetron sputtering technique. The different layers of the GSW structure and the stepped transition are fixed using transparent acrylic screws. The details of the antenna fabrication are reported in Appendix A Section S6. The optical transmittance of the fabricated leaky-wave antenna was measured using a

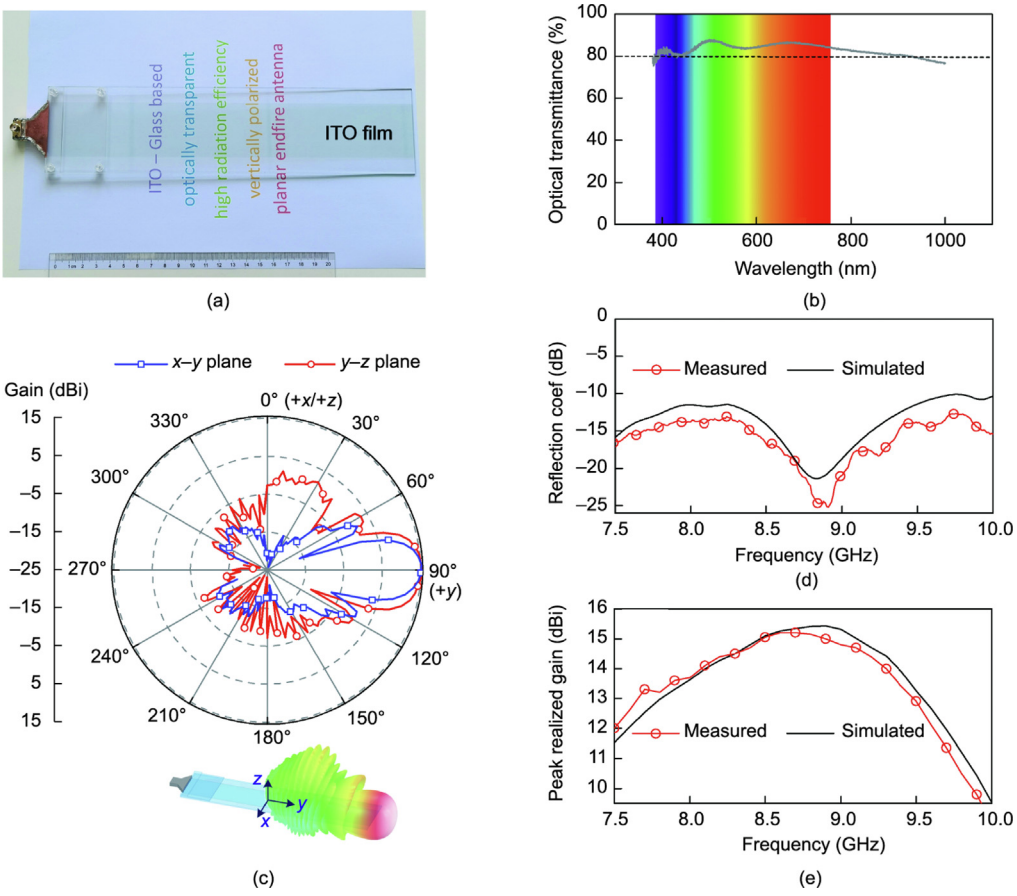

Fig. 4. Experimental characterization of the proposed optically transparent endfire leaky-wave antenna. (a) Photograph of the fabricated transparent leaky-wave antenna and (b) measured optical transmittance spectrum of the antenna. (c) Measured and simulated angular distributions of the antenna gain at f_0 = 8.6 GHz on *y*–*z* and *x*–*y* cut planes. (d, e) Measured and simulated results for (d) the reflection coefficient and (e) peak realized gain of the proposed optically transparent leaky-wave antenna. coef: coefficient.

spectrophotometer. As shown in Fig. 4(b), the average optical transmittance of the ITO-deposited region and clear-glass region is higher than 80% for wavelengths ranging from 390 to 900 nm, which confirms that the fabricated antenna is highly transparent in the visible light spectrum and a part of the near-infrared spectrum.

The radiation performance of the antenna is measured using a standard SATIMO SG-24 multi-probe system (as shown in Appendix A Fig. S5), with a typical dynamic range greater than 50 dB and an antenna gain measurement limit exceeding 30 dBi. Fig. 4(c) presents the measured angular distributions of the antenna's realized gain at 8.6 GHz on the *y*–*z* and *x*–*y* cut planes, and the numerically simulated results are presented in Appendix A Fig. S6. The simulated 3D distribution of the realized gain is shown in Fig. 3(d). Both measured and simulated results confirm that the proposed transparent leaky-wave antenna achieves a high realized gain of 15.2 dBi in the GSW's endfire direction(i.e., +*y* direction). Fig. 4(d) shows the simulated and measured reflection coefficients of the proposed transparent antenna. From 8.4 to 9.4 GHz, the measured reflection coefficient is lower than −15 dB, indicating that the power has been injected into the antenna with almost no reflection. Fig. S7 in Appendix A presents the measured and simulated radiation efficiencies of the prototyped antenna, showing that the measured and simulated radiation efficiencies at 8.6 GHz reach 66% and 69%, respectively. Fig. S8 in Appendix A reports the proportions of the reflected power, radiated power, and ohmic dissipation for the two-port TCF-grounded GSW (shown in Fig. 2(a)) and the corresponding one-port structure (shown in Fig. 3(a)) with a substrate thickness of 1.8 mm. Because the antenna port is well-matched, the antenna efficiency is primarily limited by the high sheet resistance of the TCF.

The measured and simulated results for the peak realized gain of the antenna are presented in Fig. 4(e). The measured peak realized gain in space reaches its maximum value of 15.2 dBi at 8.6 GHz. The variation in the peak realized gain is less than 1 dB from 8.15 to 9.25 GHz, which verifies the stable radiation performance of the antenna over a relatively wide bandwidth. The experiment results reveal that the degrees of freedom offered by electromagnetic mode manipulation can be exploited to overcome the imperfection of materials [61] and realize high-performance wave radiators. Fig. S9 in Appendix A displays the simulated peak realized gain and radiation efficiency of the antenna based on the ITO film with different sheet resistances. Although the antenna with high resistance ITO film would have an enhanced optical transparency, its RF radiation performance would be compromised. In this design, the ITO film with a sheet resistance of 3 $\Omega \cdot sq^{-1}$ is chosen to achieve an optical transmittance exceeding 80% and a peak antenna realized gain greater than 15 dBi.

5. OTA-based wireless transmission experiment

Optically transparent high-gain antennas provide a promising opportunity to realize high-quality wireless communication without affecting the utilization of visible light resources. Here, we showcase the application of the proposed antenna for high-quality wireless transfer of images. Fig. 5(a) demonstrates a schematic of the wireless image transfer system, in which the Tx and

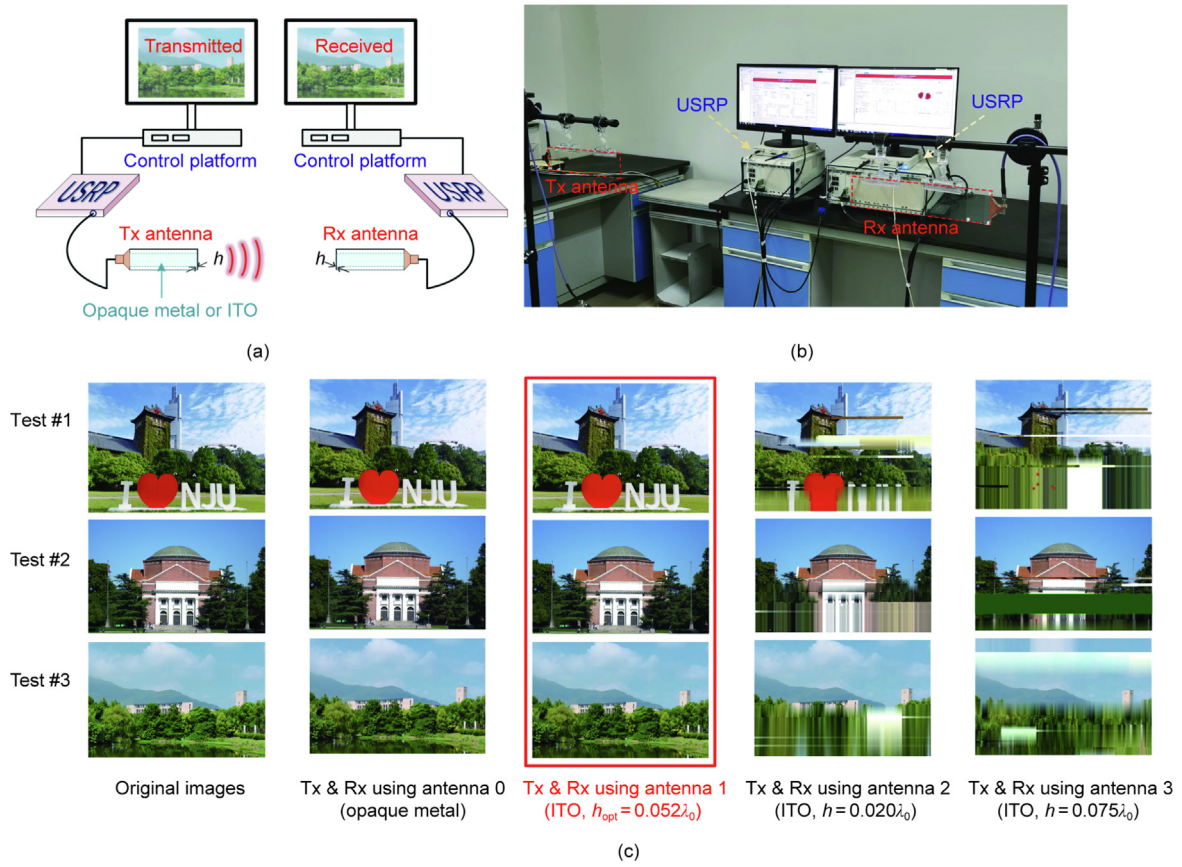

Fig. 5. Wireless image transfer based on the proposed OTA and reference antennas. (a) Schematic illustration and (b) photograph of the experiment setup, where two computer-controlled universal software radio peripheral (USRP) devices are connected with Tx and Rx antennas. (c) Original and received images in three wireless image transfer tests. For each test, wireless transmission is accomplished by using optically transparent leaky-wave antennas with different glass-slab thicknesses (h = 0.020λ_0, 0.052λ_0, and 0.075λ_0) and opaque metal-based leak-wave antenna with glass-slab thickness h = 0.052λ_0.

Rx antennas are identical. When the system operates, the control platform at the Tx end sends the image data into the universal software radio peripheral (USRP) device, through which the baseband signal with 20 MHz bandwidth is modulated onto a carrier wave at f_0 = 8.6 GHz and sent to the Tx antenna. The signal is then wirelessly transmitted, received at the Rx antenna, and demodulated by the USRP at the Rx end. Finally, the received image can be recovered on the right-hand control platform. Fig. 5(b) shows a photograph of the wireless image transfer system, which consists of two National Instruments (NI) USRP-2954R devices and two NI-PXIe-8374 control platforms. In the experiment, the Tx and Rx leaky-wave antennas are separated horizontally by a center-to-center distance of 1.5 m (i.e., 43λ_0 at 8.6 GHz), and the emission power is set to 0.01 mW. Additional information on the wireless image transfer experiment is provided in Appendix A Section S7. According to the Friis transmission equation [62], the received signal strength is directly related to the gains of the Tx and Rx antennas, and enhancing the antenna gains would improve the wireless transmission quality.

We test wirelessly transferring three images with sizes of 1020 × 1376 pixels, 900 × 1376 pixels, and 918 × 1376 pixels, as shown in the leftmost column of Fig. 5(c). For each test, we compare the transmission performance of the four types of antennas 0–3, which perform the Tx and Rx functions. Antenna 0 is an opaque leak-wave antenna (as shown in Appendix A Fig. S10) consisting of a GSW grounded by a copper sheet with R_s = 0.025 Ω·sq^{-1}. Antennas 1–3 are optically transparent leak-wave antennas grounded by ITO films with R_s = 3 Ω·sq^{-1}; they differ in glass slab thicknesses, which are h = 0.052λ_0, 0.020λ_0, and 0.075λ_0, respectively. The endfire realized gains of antennas 0–3 are 16.5, 15.2, 7.1, and 3.5 dBi, respectively. The images received at the Rx end under different antenna settings are shown in the right four columns of Fig. 5(c), and the corresponding constellation diagrams of the received signals are shown in Appendix A Fig. S11. Enclosed within the red solid frame in Fig. 5 are results obtained by using optically transparent leaky-wave antenna 1 with an optimized realized gain of 15.2 dBi. In this case, the received images exhibit no distortion compared to the original images. In contrast, much poorer image quality is observed when the wireless transceiving is based on optically transparent leaky-wave antennas 2 (or 3), which consists of an excessively thin (or thick) ITO-grounded GSW. The third and second columns of Fig. 5(c) show the images obtained via wireless transfer using the proposed optically transparent high-gain antenna (antenna 1) and its opaque metal-based counterpart (antenna 0). Evidently, the proposed design methodology can improve the performance of optically-transparent ITO-based antennas to a level comparable to that of opaque metal-based antennas, despite the ITO film used for the OTAs having sheet resistance two orders of magnitude higher than that of the opaque copper sheet used for antenna 0.

6. Discussion and conclusions

Table 1 [37,38,51–56] compares comprehensively the proposed OTA with other presentative designs developed in recent works. These directional OTAs were constructed using resonant radiation structures including patches [38,51,53,56], monopoles [55], the composite right/left-handed (CRLH) metamaterial [37], the

Table 1
Comparison of the representative directional OTA designs.

Reference	Antenna type	Optical transmittance	Area (λ_m^2)[a]	Peak realized gain (linear/dB scale[b])	Radiation efficiency[c]	Gain/area (λ_m^{-2}) (for large apertures)
[37]	CRLH metamaterial	88%[d]	2.41 × 0.30	1.85/2.67	63%	—
[51]	Patch	62%	0.41 × 0.41	1.83/2.63	43%	—
[52]	Cavity-backed slot	71%	1.61 × 1.40	3.04/4.83	45%	—
[53]	Patch	69%	0.41 × 0.41	3.37/5.28	51%	—
[56]	Coplanar patch	Not given	0.88 × 0.44	1.00/0.00	69%	—
[54]	Slot with ground	71%	2.05 × 2.05	3.55/5.50	60%	0.84
[38]						
Antenna 1	Patch array	88%[d]	1.96 × 4.85	4.63/6.66	24%	0.49
Antenna 2	Patch array	88%[d]	1.96 × 4.85	8.24/9.16	41%	0.87
[55]	Monopole array	86%	1.95 × 3.90	9.33/9.70	61%	1.23
This work	Leaky-wave antenna	80%	7.91 × 1.89	33.11/15.20	66%	2.21

CRLH: composite right/left-handed.
[a] λ_m is the wavelength at the frequency of maximum realized gain.
[b] dB-scale gain = 10·lg (linear-scale gain).
[c] The radiation efficiency is given at the frequency of maximum realized gain.
[d] These works report optical transmittance of the radiation structure alone.

cavity-backed slot [52], and the ground-backed slot [54]. As shown in Table 1 [37,38,51–56], the proposed OTA design based on the low-loss leaky-wave structure offers a competitive optical transmittance, enhanced radiation efficiency, and an outstanding antenna realized gain which, on the linear scale, is more than 3.5 times higher than those of other designs. Besides that, the proposed OTA features a significantly improved aperture usage rate (i.e., the ratio of the maximum linear-scale realized gain to the antenna's electrical area), which reflects the overall advantage of the proposed design.

Recently, significant efforts have been devoted to engineering wave confinement in artificial electromagnetic structures, such as spoof surface plasmon polariton (SSPP) structures [63–65]. In this study, we leveraged wave confinement engineering to determine an optimal radiation state for an optically transparent leaky-wave structure, in which the dissipation on lossy TCFs is effectively suppressed. As an emerging concept and technology, multifunctional metasurfaces [66–68], which enable the flexible manipulation of wave magnitudes, phases, and polarizations, have also gained great interest. Incorporating metasurfaces into the optically transparent leaky-wave antenna design for OTA's functionalities enhancement will be a future research topic.

In conclusion, this paper demonstrated the theory and methodology for maximizing the endfire radiation gain for a lossy TCF, addressing the problem that RF radiators made of TCFs commonly exhibit low efficiency and low gain. Our method leveraged the manipulation of the leaky-wave mode in a TCF-grounded GSW, which mitigates the attenuating effect of TCFs without the need to improve TCFs' conductivity. By controlling the transverse wave confinement in the TCF-grounded GSW, strong field confinement near the lossy TCF is avoided, which substantially suppresses the TCF-loss-induced attenuation. Subsequently, the optimal GSW-thickness condition was derived to minimize the total attenuation caused by material dissipation and wave leakage, which provides a unique opportunity for generating high-gain radiation on a lossy TCF. Exploiting this low-attenuation leaky-wave state, we proposed a transparent antenna featuring an extended aperture size of $7.9\lambda_0 \times 1.9\lambda_0$ and high optical transmittance (> 80%). Solid experimental results verified the prototyped antenna's competitive radiation performances, achieving an optimal realized gain of 15.2 dBi and a competitive radiation efficiency of 66%. In essence, this study provides an effective mode-manipulation approach for mitigating the intrinsic loss issue of TCFs, creating a pathway for realizing high-performance OTAs with promising applications in future ubiquitous wireless communication and sensing.

Acknowledgments

The authors acknowledge the support partially from the National Natural Science Foundation of China (62301162, 62401386, 62071125, 62071187, 62022045, and U22B2016), partially from the Industry–Education Cooperation Project of Fujian Province (#2022H6018), partially from the Fujian Provincial Natural Science Foundation of China (2023J01058), partially from the National Key Research and Development Program of China (2021YFA0716601 and 2022YFE0115500), and partially from the Startup Funding of Fuzhou University (XRC-23007).

Compliance with ethics guidelines

Ziheng Zhou, Yongjian Zhang, Yilin Zheng, Ke Chen, Yueming Gao, Yuehe Ge, Yue Li, Yijun Feng, and Zhizhang (David) Chen declare that they have no conflict of interest or financial conflicts to disclose.

Appendix A. Supplementary data

Supplementary data to this article can be found online at https://doi.org/10.1016/j.eng.2024.09.014.

References

[1] Griffiths DJ. Introduction to electrodynamics. 3rd ed. Upper Saddle River: Prentice-Hall; 1999.
[2] Balanis CA. Antenna theory: analysis and design. 3rd ed. Hoboken: John Wiley & Sons; 2005.
[3] Mittra R, Nasri A, Arya RK. Wide-angle scanning antennas for millimeter-wave 5G applications. Engineering 2022;11:60–71.
[4] Khan AN, Cha YO, Giddens H, Hao Y. Recent advances in organ specific wireless bioelectronic devices: perspective on biotelemetry and power transfer using antenna systems. Engineering 2022;11:27–41.
[5] Baek WK, Jung HS. Precise three-dimensional deformation retrieval in large and complex deformation areas via integration of offset-based unwrapping and improved multiple-aperture SAR interferometry: application to the 2016 Kumamoto earthquake. Engineering 2020;6:927–35.
[6] Ghasr MT, Horst MJ, Dvorsky MR, Zoughi R. Wideband microwave camera for real-time 3-D imaging. IEEE Trans Antennas Propag 2017;65:258–68.
[7] Ito K. Compelling challenges in antenna technologies for future medical applications. Engineering 2022;11:15–7.
[8] Liu J, Jackson DR, Long Y. Substrate integrated waveguide (SIW) leaky-wave antenna with transverse slots. IEEE Trans Antennas Propag 2012;60:20–9.
[9] Hou Y, Li Y, Zhang Z, Iskander MF. All-metal endfire antenna with high gain and stable radiation pattern for the platform-embedded application. IEEE Trans Antennas Propag 2019;67:730–7.
[10] Zhang X, Sun L, Li Y, Zhang ZA. Grooved half-mode waveguide leaky-wave antenna for vertically-polarized endfire radiation. IEEE Trans Antennas Propag 2021;69:8229–36.

[11] Liu J, Jackson DR, Li Y, Zhang C, Long Y. Investigations of SIW leaky-wave antenna for endfire-radiation with narrow beam and sidelobe suppression. IEEE Trans Antennas Propag 2014;62:4489–97.
[12] Zhang W, Li Y, Zhang Z. A Substrate integrated slot leaky-wave antenna for point-to-point communication. IEEE Trans Antennas Propag 2022;70:9888–93.
[13] Sun L, Liu P, Li Y, Chang L, Wei K, Zhang Z. Metal strip endfire antenna based on TE_1 leaky-wave mode. IEEE Trans Antennas Propag 2020;68:5916–23.
[14] Ge S, Zhang Q, Rashid AK, Zhang Y, Wang H, Murch RD. General design technique for high-gain traveling-wave endfire antennas using periodic arbitrary-phase loading technique. IEEE Trans Antennas Propag 2021;69:3094–105.
[15] Sievenpiper DF. Superluminal waveguides based on non-foster circuits for broadband leaky-wave antennas. IEEE Antennas Wirel Propag Lett 2011;10:231–4.
[16] Li M, Xiao SQ, Sievenpiper DF. Polarization-insensitive holographic surfaces with broadside radiation. IEEE Trans Antennas Propag 2016;64(12):5272–80.
[17] Zhang Y, Li Y. Wideband microstrip antenna in small volume without using fundamental mode. Electromag Sci 2023;1(2):0020073.
[18] Li H, Zhou Z, Zhao Y, Li Y. Low-loss beam synthesizing network based on epsilon-near-zero (ENZ) medium for on-chip antenna array. Chip 2023;2:100049.
[19] Li H, Zhou Z, He Y, Sun W, Li Y, Liberal I, et al. Geometry-independent antenna based on Epsilon-near-zero medium. Nat Commun 2022;13:3568.
[20] Hu PF, Leung KW, Luk KM, Pan YM, Zheng SY. Diversity glass antennas for tri-band WiFi applications. Engineering 2023;23:157–69.
[21] Zhang Y, Li Y, Zhang W, Zhang Z, Feng Z. Omnidirectional antenna diversity system for high-speed onboard communication. Engineering 2022;11:72–9.
[22] Wang ZX, Yang H, Shao R, Wu JW, Liu G, Zhai F, et al. A planar 4-bit reconfigurable antenna array based on the design philosophy of information metasurfaces. Engineering 2022;17:64–74.
[23] Eleftheriades GV, Kim M, Ataloglou VG, Dorrah AH. Prospects of Huygens' metasurfaces for antenna applications. Engineering 2022;11:21–6.
[24] Yang W, Chen K, Zhao J, Jiang T, Feng Y. A wideband high-efficiency transmit-reflect-array antenna for bidirectional radiations with distinct circular polarizations based on a metasurface. IEEE Trans Antenna Propag 2023;71:3695–700.
[25] Silva ZJ, Valenta CR, Durgin GD. Optically transparent antennas: a survey of transparent microwave conductor performance and applications. IEEE Antennas Propag Mag 2021;63:27–39.
[26] Lee SY, Choo M, Jung S, Hong W. Optically transparent nano-patterned antennas: a review and future directions. Appl Sci 2018;8:901.
[27] Alobaidi OR, Chelvanathan P, Tiong SK, Bais B, Uzzaman MA, Amin N. Transparent antenna for green communication feature: a systematic review on taxonomy analysis, open challenges, motivations, future directions and recommendations. IEEE Access 2022;10:12286–321.
[28] Zu HR, Wu B, Chen B, Li WH, Su T, Liu Y, et al. Optically and radiofrequency-transparent metadevices based on quasi-one-dimensional surface plasmon polariton structures. Nat Electron 2023;6:525–33.
[29] Lombardi JP, Malay RE, Schaffner JH, Song HJ, Huang MH, Pollard SC, et al. Copper transparent antennas on flexible glass by subtractive and semi-additive fabrication for automotive applications. In: Proceedings of IEEE 68th Electronic Components and Technology Conference; 2018 May 29– Jun 1; San Diego, CA, USA; 2018.
[30] Yasan E, Song HJ, Talty T, Schaffner JH, Carper D, Bekaryan A. Field performance of a novel wideband optically transparent GNSS antenna. In: Proceedings of 2019 IEEE International Symposium on Antennas and Propagation and USNC-URSI Radio Science Meeting; 2019 Jul 7–12; Atlanta, GA, USA; 2019.
[31] Potti D, Tusharika Y, Alsath MGN, Kirubaveni S, Kanagasabai M, Sankararajan R, et al. A Novel optically transparent UWB antenna for automotive MIMO communications. IEEE Trans Antennas Propag 2021;69:3821–8.
[32] Sun YX, Wu D, Fang XS, Ren J. On-glass grid structure and its application in highly-transparent antenna for Internet of Vehicles. IEEE Trans Veh Technol 2023;72:93–101.
[33] Liu ZG, Zhang C, Yin JR, Lu WB. Multifunctional low-profile Fabry–Perot resonator antenna integrated with solar cells. IEEE Trans Antennas Propag 2022;70:7175–80.
[34] Xi B, Liang X, Chen Q, Wang K, Geng J, Jin R. Optical transparent antenna array integrated with solar cell. IEEE Antennas Wirel Propag Lett 2020;19:457–61.
[35] Ha TD, Zhu L, Alsaab N, Chen PY, Guo JL. Optically transparent metasurface radome for RCS reduction and gain enhancement of multifunctional antennas. IEEE Trans Antennas Propag 2023;71:67–77.
[36] Oh J, Kim B, Yoon S, Kim K, Sung EJ, Oh J. High-gain millimeter-wave antenna-in-display using non-optical space for 5G smartphones. IEEE Trans Antennas Propag 2023;71:1458–68.
[37] Kim M, Lee D, Oh Y, Lee JY, Kim B, Park J. Antenna-on-display concept on an extremely thin substrate for sub-6 GHz wireless applications. IEEE Trans Antennas Propag 2022;70:5929–34.
[38] Park J, Lee SY, Kim J, Park D, Choi W, Hong W. An optically invisible antenna-on-display concept for millimeter-wave 5G cellular devices. IEEE Trans Antennas Propag 2019;67:2942–52.
[39] Hong W, Lim S, Ko S, Kim YG. Optically invisible antenna integrated within an OLED touch display panel for IoT applications. IEEE Trans Antennas Propag 2017;65:3750–5.
[40] Li S, Tian M, Gao Q, Wang M, Li T, Hu Q, et al. Nanometre-thin indium tin oxide for advanced high-performance electronics. Nat Mater 2019;18:1091–7.
[41] Datta RS, Syed N, Zavabeti A, Jannat A, Mohiuddin M, Rokunuzzaman M, et al. Flexible two-dimensional indium tin oxide fabricated using a liquid metal printing technique. Nat Electron 2020;3:51–8.
[42] Li T, Chen K, Ding G, Zhao J, Jiang T, Feng Y. Optically transparent metasurface salisbury screen with wideband microwave absorption. Opt Express 2018;26:34384–95.
[43] Chen B, Wu B, Zu HR, Hou JQ, Su T. Experimental demonstration of high optically transparent reflectarrays using fine metal line structure. IEEE Trans Antennas Propag 2022;70:10504–11.
[44] Putzke C, Guo C, Plisson V, Kroner M, Chervy T, Simoni M, et al. Layered metals as polarized transparent conductors. Nat Commun 2023;14:3147.
[45] Fan RH, Peng RW, Huang XR, Li J, Liu Y, Hu Q, et al. Transparent metals for ultrabroadband electromagnetic waves. Adv Mater 2012;24:1980–6.
[46] Ding C, Liu L, Luk KM. An optically transparent dual-polarized stacked patch antenna with metal-mesh films. IEEE Antennas Wirel Propag Lett 2019;18:1981–5.
[47] Song HJ, Schaffner JH, Son KA, Moon JS. Optically transparent Ku-band silver nanowire frequency selective surface on glass substrate. In: Proceedings of 2014 IEEE Antennas and Propagation Society International Symposium; 2014 Jul 6–11; Memphis, TN, USA; 2014.
[48] Song HJ, Schaffner JH, Bekaryan A, O'Connor K, Tombs T, Talty T, et al. Roll-to-roll printed transparent applique antennas. In: Proceedings of 2018 IEEE International Symposium on Antennas and Propagation & USNC/URSI National Radio Science Meeting; 2018 Jul 8–13; Boston, MA, USA; 2018.
[49] Tung PD, Jung CW. Optically transparent wideband dipole and patch external antennas using metal mesh for UHD TV applications. IEEE Trans Antennas Propag 2020;68:1907–17.
[50] Yao Y, Chen W, Chen X, Yu J. Design of optically transparent antenna with directional radiation patterns. Int J Antenn Propag 2017;8125432.
[51] Hong S, Kim Y, Jung CW. Transparent microstrip patch antennas with multilayer and metal-mesh films. IEEE Antennas Wirel Propag Lett 2017;16:772–5.
[52] Shi Y, Wang WJ, Hu TT. A transparent SIW cavity-based millimeter-wave slot antenna for 5G communication. IEEE Antennas Wirel Propag Lett 2022;21:1105–9.
[53] Kang SH, Jung CW. Transparent patch antenna using metal mesh. IEEE Trans Antennas Propag 2018;66:2095–100.
[54] Hautcoeur J, Colombel F, Himdi M, Castel X, Cruz EM. Large and optically transparent multilayer for broadband H-shaped slot antenna. IEEE Antennas Wirel Propag Lett 2013;12:933–6.
[55] Qiu H, Liu H, Jia X, Jiang ZY, Liu YH, Xu J, et al. Compact, flexible, and transparent antennas based on embedded metallic mesh for wearable devices in 5G wireless network. IEEE Trans Antennas Propag 2021;69:1864–73.
[56] Song HJ, Hsu TY, Sievenpiper DF, Hsu HP, Schaffner J, Yasan E. A method for improving the efficiency of transparent film antennas. IEEE Antennas Wirel Propag Lett 2008;7:753–6.
[57] Haraty MR, Naser-Moghadasi M, Lotfi-Neyestanak AA, Nikfarjam A. Improving the efficiency of transparent antenna using gold nanolayer deposition. IEEE Antennas Wirel Propag Lett 2016;15:4–7.
[58] Zhang L, Zhou Y, Guo L, Zhao W, Barnes A, Zhang HT, et al. Correlated metals as transparent conductors. Nat Mater 2016;15:204–10.
[59] Pozar DM. Microwave engineering chapter 3. 4th ed. Hoboken: John Wiley & Sons; 2011.
[60] Collin RE. Field theory of guided waves chapter 4. 2nd ed. Piscataway: IEEE Press; 1991.
[61] Li Y, Liberal I, Engheta N. Structural dispersion–based reduction of loss in epsilon-near-zero and surface plasmon polariton waves. Sci Adv 2019;5:eaav3764.
[62] Bertoni HL. Radio propagation for modern wireless systems. Upper Saddle River: Prentice-Hall; 2000.
[63] Pendry JB, Martín-Moreno L, Garcia-Vidal FJ. Mimicking surface plasmons with structured surfaces. Science 2004;305(5685):847–8.
[64] Shen X, Cui TJ, Martin-Cano D, Garcia-Vidal FJ. Conformal surface plasmons propagating on ultrathin and flexible films. Proc Natl Acad Sci USA 2013;110(1):40–5.
[65] Gao X, Ma Q, Gu Z, Cui WY, Liu C, Zhang J, et al. Programmable surface plasmonic neural networks for microwave detection and processing. Nat Electron 2023;6:319–28.
[66] Li J, Yuan Y, Wu Q, Zhang K. Bi-isotropic Huygens' metasurface for polarization-insensitive cross-polarization conversion and wavefront manipulation. IEEE Trans Antennas Propag 2024;72(3):2445–54.
[67] Yuan Y, Wu Q, Burokur SN, Zhang K. Chirality-assisted phase metasurface for circular polarization preservation and independent hologram imaging in microwave region. IEEE Trans Microw Theory Techn 2023;71(8):3259–72.
[68] Yuan Y, Zhang K, Ratni B, Song Q, Ding X, Wu Q, et al. Independent phase modulation for quadruplex polarization channels enabled by chirality-assisted geometric-phase metasurface. Nat Commun 2020;11:4168.